On the accurate description of uranium metallic phases: a MEAM interatomic potential approach

2014 Modelling Simul. Mater. Sci. Eng. 22 055019

(http://iopscience.iop.org/0965-0393/22/5/055019)

IOP Publishing Modelling and Simulation in Materials Science and Engineering

Modelling Simul. Mater. Sci. Eng. **22** (2014) 055019 (19pp) doi:10.1088/0965-0393/22/5/055019

On the accurate description of uranium metallic phases: a MEAM interatomic potential approach

J R Fernández[1,2,3] **and M I Pascuet**[3]

[1] Dep. Materiales, CAC-CNEA, Av. Gral. Paz 1499, (B1650KNA) San Martín, Buenos Aires, Argentina
[2] Instituto Sabato, UNSAM/CNEA, Av. Gral. Paz 1499, 1650 San Martín, Buenos Aires, Argentina
[3] CONICET, Av. Rivadavia 1917 (1033) CABA, Buenos Aires, Argentina

E-mail: julrfern@cnea.gov.ar

Received 3 February 2014, revised 24 April 2014
Accepted for publication 9 May 2014
Published 6 June 2014

Abstract

A new interatomic potential in the framework of the modified embedded atom method (MEAM) to model U metal is presented. The potential acceptably reproduces the lattice parameters and cohesive energy of the orthorhombic αU. The relative stability of the experimentally observed phase at low temperatures with respect to several other structures (bct, bcc, simple cubic, tetragonal βNp, fcc and hcp) is also taken into account. Intrinsic point defect properties compare reasonably well with data from the literature. To determine the quality of the interaction, the potential is used to study a number of properties for the pure metal at finite temperatures and the results are compared with the available data. The obtained allotropic αU $\leftrightarrow$ γU transformation and melting temperatures are in good agreement with experimental values. Based on the simulations, a new αU $\leftrightarrow$ γU transformation mechanism is proposed.

Keywords: uranium, MEAM interatomic potential, computer simulation

(Some figures may appear in colour only in the online journal)

1. Introduction

The purpose of replacing traditional high-density nuclear fuel U alloys, which has been under discussion for several years, is to increase the burning of fissile material and decrease the amount of high-level waste [1–3]. In practice, the U–Mo alloy is dispersed in an Al matrix which acts as a mechanical support and allows for the fast transmission of heat generated by fission. However, there are some problems due to the formation of intermetallic phases at the

Al/U–Mo interface, the formation dynamics of which is of interest for both technological and academic purposes [4–6]. This fuel replacement plan created renewed interest in the study of metallic U and its alloys.

As for the case of many actinides, U has very unique properties due to its f electrons [7]. At normal pressures, the pure metal undergoes different allotropic transformations as temperature increases. At low temperatures, the orthorhombic α phase (strukturbericht A20) is stable for $T < 935\,\mathrm{K}$. At intermediate temperatures ($935\,\mathrm{K} < T < 1045\,\mathrm{K}$), the β phase occurs, which has a complex tetragonal structure containing 30 atoms per unit cell (A_b). Finally, the body-centered cubic (bcc) γ phase (A2) is stable up to the melting point ($T_m = 1405\,\mathrm{K}$) [8, 9].

Investigations of the structure and properties of U and its alloys have been performed by a number of authors using *ab initio* methods. Söderlind *et al*'s [10–13] early works studied many of the structural properties of light actinides in order to establish common trends among f-electron metals. Taylor [14] calculated several structural and thermodynamic properties for αU and reported the first studies of the vacancy formation energy and the (0 0 1) surface in the same structure. The contemporary work of Xiang *et al* [15] showed studies for all of the allotropic phases and the vacancy in γU. More recently, Li *et al* [16] reported on the structural parameters and energies of the experimentally observed phases and other metastable phases, and discussed the different structural possibilities for the βU phase. On the other hand, Beeler *et al* [17, 18] have also obtained the lattice parameters and elastic constants of all three solid phases of U, and have characterized the vacancy and self-interstitial point defects in αU and γU. Finite temperature calculations have also been performed for this metal. Quantum molecular dynamics (MD) over a range of pressures and temperatures have been carried out by Hood *et al* [19], who characterized the αU, γU and liquid phases. An explanation for the temperature stabilization of the bcc phase of actinide metals was proposed by Söderlind *et al* [20] by means of a self-consistent *ab initio* lattice dynamics scheme. Recently, there has been increasing interest in the study of U alloys with other transition elements, mainly Zr and Mo. Huang and Wirth [21] reported calculations for the mobility of point defects in the low-temperature phase of U in the presence of Zr and other fission products. Regarding the bcc high-temperature phase, Landa *et al* [22] provided a rational explanation for the higher constituent redistribution in the U–Zr alloys compared to U–Mo by comparing the calculated heat of formation in U–Zr and U–Mo over the whole composition range. The list is not exhaustive and only a sample of the works is shown here.

Nevertheless, first-principles methods are only useful for relatively small systems still cost a huge computational effort. For larger systems, a more reasonable option is the use of semi-empirical potentials. There has been increased interest in developing these interaction schemes. One of the first attempts to model metallic U by means of an embedded atom method (EAM) interatomic potential was made by Pascuet *et al* [23–25], hereafter referred to as EAM1. The obtained potential reproduced some structural properties of the α phase and was able to transform from the α phase to the γ phase in the course of a MD simulation, although at a lower temperature than that observed by experiments. Belashchenko *et al* [26] developed an appropriate EAM interaction that was mainly intended to describe the properties of the liquid but which was also able to represent some aspects of γU. A much more accurate interaction was determined by Smirnova *et al* [27], who obtained an EAM potential (EAM2) by using the force-matching method, which they claim to be adequate to model αU, γU and liquid phases. On the other hand, Beeler *et al* [28] were the first to develop a modified EAM (MEAM) interatomic potential to model the bcc properties of the γU phase, but it does not seem to be appropriate for describing αU as reported by the authors. Other interaction schemes have been investigated, like the charge optimized many body (COMB) classical interaction for orthorhombic U derived by Li *et al* [29], although some limitations are found.

In this paper, an interatomic potential of the MEAM type [30] for pure U is developed for use in future studies in Al–Mo–U alloys. This interaction scheme is an improvement over previous ones [31, 32], since it takes into account the atomic directional bonding. The addition of angular forces is found to be critical for reproducing the behavior of complex crystal structures, like those found in technologically important U alloys.

In section 2, the MEAM formalism is described. Section 3 is devoted to the fitting method for all of the model parameters. The different physical properties calculated using the obtained potential through static and dynamic simulations at finite temperatures are reported in section 4. All of the simulations are performed with LAMMPS [33], a freely available computation code which integrates a large number of force fields and calculation algorithms. Finally, in section 5, we draw some conclusions.

2. Formalism

A full description of the original MEAM formalism has been published in the report of Gullett *et al* [34]. In the MEAM, the total energy of a unary system is approximated as

$$E = \sum_i F(\bar{\rho}_i) + \frac{1}{2}\sum_{j\neq i}\phi(R_{ij}), \tag{1}$$

where F is the embedding function, $\bar{\rho}_i$ is the background electron density at site i and $\phi(R_{ij})$ is the pair interaction between atoms i and j, separated by a distance R_{ij}. The energy system is given by the calculation of the F and ϕ functions.

The embedding function is given as follows:

$$F(\bar{\rho}) = AE_c\frac{\bar{\rho}}{\bar{\rho}^0}\ln\left[\frac{\bar{\rho}}{\bar{\rho}^0}\right], \tag{2}$$

where A is an adjustable parameter, E_c is the cohesion energy and $\bar{\rho}^0$ is the background electron density for a reference structure. In the present work, the bcc structure will be taken as the reference. The background electron density $\bar{\rho}_i$ is composed of a spherically symmetric partial electron density $\rho_i^{(0)}$ and the angular contributions $\rho_i^{(1)}$, $\rho_i^{(2)}$ and $\rho_i^{(3)}$:

$$(\rho_i^{(0)})^2 = \left[\sum_{j\neq i}\rho_j^{\alpha(0)}(R_{ij})\right]^2, \tag{3a}$$

$$(\rho_i^{(1)})^2 = \sum_\alpha\left[\sum_{j\neq i}\frac{R_{ij}^\alpha}{R_{ij}}\rho_j^{\alpha(1)}(R_{ij})\right]^2, \tag{3b}$$

$$(\rho_i^{(2)})^2 = \sum_{\alpha,\beta}\left[\sum_{j\neq i}\frac{R_{ij}^\alpha R_{ij}^\beta}{R_{ij}^2}\rho_j^{\alpha(2)}(R_{ij})\right]^2 - \frac{1}{3}\left[\sum_{j\neq i}\rho_j^{\alpha(2)}(R_{ij})\right]^2, \tag{3c}$$

$$(\rho_i^{(3)})^2 = \sum_{\alpha,\beta,\gamma}\left[\sum_{j\neq i}\frac{R_{ij}^\alpha R_{ij}^\beta R_{ij}^\gamma}{R_{ij}^3}\rho_j^{\alpha(3)}(R_{ij})\right]^2 - \frac{3}{5}\sum_\alpha\left[\sum_{j\neq i}\frac{R_{ij}^\alpha}{R_{ij}}\rho_j^{\alpha(3)}(R_{ij})\right]^2. \tag{3d}$$

R_{ij} is the distance between the i and j atoms, R_{ij}^α is the α component and $\rho_j^{\alpha(h)}$ is the atomic electron density of the j atom located at a distance R_{ij} from the i atom:

$$\rho^{\alpha(h)}(R) = \exp[-\beta^{(h)}(R/r_e - 1)], \tag{4}$$

where $\beta^{(h)}$ are adjustable parameters and r_e is the nearest-neighbor distance in the equilibrium reference structure. The partial electron densities are combined:

$$\Gamma_i = \sum_{h=1}^{3} t^{(h)} [\rho_i^{(h)} / \rho_i^{(0)}]^2, \tag{5}$$

where $t^{(h)}$ are adjustable parameters. The total electron density at site i is evaluated as

$$\bar{\rho}_i = \rho_i^{(0)} G(\Gamma_i) \tag{6}$$

where the $G(\Gamma)$ function can take different expressions [35]. In the present case of uranium,

$$G(\Gamma) = 2/(1 + e^{-\Gamma}). \tag{7}$$

There is no specific form for the pair interaction $\phi(R)$ in the MEAM formalism. Its value is computed by means of the total energy (equation (1)) and the embedding function as a function of distance R (equation (2)) as follows.

The total energy per atom for the reference structure is obtained with a variation of the universal state equation of Rose *et al* [36] as a function of R.

$$E^a(R) = -E_c \left(1 + a^* + d\frac{r_e}{R}a^{*3}\right) e^{-a^*} \tag{8}$$

where d is an adjustable parameter,

$$a^* = \alpha(R/r_e - 1) \tag{9}$$

and

$$\alpha = (9B\Omega/E_c)^{1/2} \tag{10}$$

where B is the bulk modulus and Ω is the equilibrium atomic volume. The parameter d of equation (8) can be used to slightly modify the shape of the total energy E^a by choosing the different values d_1 or d_2, whenever a^* is positive (expansion) or negative (contraction), respectively, as implemented in the LAMMPS code [33]. To define the pair potential $\phi(R)$, the total energy E^a is expressed in terms of the function F and the pair potential, considering up to second neighbor interactions [37] in the reference structure:

$$E^a(R) = F[\bar{\rho}^0(R)] + (Z_1/2)\phi(R) + (Z_2 S/2)\phi(aR), \tag{11}$$

where Z_i is the number of neighbors in the i shell, a is the ratio between the first and second neighbor distances and S is the screening factor. Lee *et al* [37] have shown the details for extracting $\phi(R)$ from equation (11). The screening factor S represents the influence of the neighbor atoms k on the interaction between i and j. For each neighbor atom k it is possible to calculate a C factor:

$$x^2 + \frac{1}{C}y^2 = \frac{R_{ij}^2}{4}, \tag{12}$$

where x and y are the coordinates of the atom k with respect to the ellipse defined by the positions i, j and k. The screening of the k atom varies gradually in the range $C_{min} < C < C_{max}$. If $C < C_{min}$, then the screening is total ($S = 0$) and there is no direct interaction between i and j, while if $C > C_{max}$ the interaction is independent of k ($S = 1$) [35].

Table 1. Optimized parameters for the U-MEAM interatomic potential.

α	4.150 266 9	$t^{(1)}$	3.460 123 1
A	0.807 662 6	$t^{(2)}$	1.524 604 7
$\beta^{(0)}$	6.084 075 6	$t^{(3)}$	3.112 947 7
$\beta^{(1)}$	5.286 634 3	d_1	−0.256 5517
$\beta^{(2)}$	8.014 071 2	d_2	0.306 801 2
$\beta^{(3)}$	4.444 697 7	$C_{\min}$	0.327 255 0
A(Å)	3.463 412 0	$C_{\max}$	3.358 370 9
E_c (eV)	5.397 236 0		

3. Determination of parameters

The parameters of the model are determined by minimizing the objective function:

$$Q = \sum_i w_i \frac{(q_i^{\text{ref}} - q_i^{\text{calc}})^2}{(q_i^{\text{ref}})^2}, \tag{13}$$

where q_i^{ref} are reference values, q_i^{calc} are values calculated using the MEAM potential and w_i are the corresponding weights. The minimization is carried out using the downhill simplex method [38], a very robust iterative algorithm in which the derivatives of Q are not required. First, an initial set of parameters is chosen in order to obtain all of the target values (energies, lattice parameters, elastic constants, etc). The obtained values are then compared with the references by evaluating equation (13) and a new set of parameters is calculated. At each iteration, all of the calculated properties are fully relaxed by using the LAMMPS code [33]. The best set of optimized parameters, achieved after several initial tries, is shown in table 1. The fully relaxed values calculated with the best set of values and the reference values (in bold) are compared in tables 2 and 3. Experimental values at low temperatures, when available, are usually preferred as reference values. Otherwise, first-principles values are chosen. It is worth noting that all references correspond ideally to $T = 0$ K. Values obtained with the potential EAM1 [25], the EAM2 of Smirnova *et al* [27] and those extracted from the work of Li *et al* [29] are also reported for comparison with other interaction frameworks.

The fitting process is a trade off, as an exact reproduction of all of the target properties has not been possible with any of the optimized set of parameters. The main emphasis is placed on the vacancy mobility [21] and on the hierarchy of energies for the available structures as obtained by first-principles calculations [11, 13, 39]. All of the sets that stabilize the body-centered tetragonal (bct) structure with $c/a < 1$ against bcc [11] lead to an incorrect order of structure energies or completely wrong values of the vacancy jumps and therefore have been disregarded. Instead, a very low energy bct with $c/a > 1$ (named *struckturbericht* A6 in table 2) is easily obtained and care must be taken to force it to be less stable than the αU fundamental structure. Finally, the target values of the elastic constants are given a relatively low weight. As a result of these fitting characteristics, the lattice parameters and elastic behavior of αU are reproduced only moderately well, and the vacancy formation energy is much higher than suggested by first-principles calculations. These downturns are a worthwhile price to pay in order to ensure good stability for the αU structure at higher temperatures and are an appropriate description of the different vacancy jumps.

Table 2. Calculated (MEAM) and reference values (experimental and calculated by first principles, Exp and FP) for lattice parameters; cohesion energies E_c; and vacancy formation volume V_v^f (in terms of the atomic volume Ω) and formation E_v^f and migration E_v^m energies for neighbor jumps to the fourth shell (shell numbers in parenthesis, explanation in section 4.4) for αU. The energy differences ΔE with several other structures from αU are shown. Results for other interatomic potentials from the literature are also reported. Values shown in bold are used in the fitting of the potential parameters.

Structure	Property	MEAM	EAM1 [25]	EAM2 [27]	COMB [29]	FP	Exp	w
A20,ort	a(Å)	2.721	2.775	2.824	2.7776	2.845 [13] 2.797 [14] 2.798 [21] 2.790 [40]	**2.836** [43]	5×10^3
	b(Å)	6.381	6.072	5.762	6.1519	5.818 [13] 5.867 [14] 5.866 [21] 5.866 [40]	**5.867** [43]	5×10^3
	c(Å)	4.858	4.936	4.941	4.7974	4.996 [13] 4.893 [14] 4.899 [21] 4.872 [40]	**4.935** [43]	5×10^3
	y	0.093	0.104	0.105	0.0921	0.103 [13] 0.098 [14] 0.097 [21] 0.102 [40]	**0.102** [43]	5×10^3
	E_c (eV/at)	5.547	5.773	4.284		—	**5.550** [44]	10^5
	V_v^f(Ω)	0.621	0.555	0.822		—		
	E_v^f (eV)	2.597	1.358	2.13		1.95 [14] 1.86 [17] **1.69** [21]		10^2
	E_v^m	0.299	0.29	0.563		**0.33** [21]		10^2
	E_v^m	0.361	0.17	0.410		**0.33** [21]		10^2
	E_v^m	1.524	0.71	1.089		1.58 [21]		
	E_v^m	1.252	0.60	1.311		1.24 [21]		
A1,fcc	a(Å)	4.481	4.328	4.226		**4.48** [14] 4.30 [41] 4.44 [16]		5×10^3
	$\Delta E_{fcc-ort}$ (eV/at)	0.255	0.169	0.328		**0.26** [13] 0.39 [16]		10^5
A2,bcc	a(Å)	3.463	3.485	3.553	3.509	3.428 [17] 3.43 [14] **3.45** [42] 3.46 [13] 3.46 [16]	3.47 [45]	5×10^3
	$\Delta E_{bcc-ort}$ (eV/at)	0.150	0.007	0.053	0.45	**0.22** [13] 0.28 [16]		10^5

Table 2. (Continued.)

A3,hcp	a(Å)	2.990	3.060	2.945	2.99 [16]	
	c/a	1.916	1.633	1.732	1.85 [16]	
	$\Delta E_{\mathrm{hcp-ort}}$ (eV/at)	0.255	0.169	0.24	**0.24** [13] 0.23 [16]	10^5
A_d,βNp	a(Å)	4.908	4.928	5.002	4.9 [11]	
	c/a	0.706	0.707	0.637	0.69 [11]	
	u	0.376	0.5	0.352	0.4 [11]	
	$\Delta E_{\beta\mathrm{Np-ort}}$ (eV/at)	0.078	0.007	0.015	**0.14** [11]	5×10^3
A_h,sc	a(Å)	2.635	2.737	2.768	2.7 [39]	
	$\Delta E_{\mathrm{sc-ort}}$ (eV/at)	0.101	0.194	0.352	0.15 [39] $>$**0.1**	5×10^3
A6,bct	a(Å)	2.722	2.775	2.779	2.82 [11]	
	c/a	2.124	1.946	1.851	1.85 [11]	
	$\Delta E_{\mathrm{bct-ort}}$ (eV/at)	0.014	0	0.054	0.15 [11] $>$**0.1**	5×10^3

Table 3. Calculated values for the elastic constants C_{ij} (GPa) and bulk modulus B (GPa) for αU with the present potential (MEAM). Results from other interaction schemes are also shown. Experimental values (Exp) in bold are included in the fitting process.

	MEAM	EAM1 [25]	EAM2 [27]	COMB [29]	Exp [46]	w
C_{11}	436.1	182	151	257.6	**214.7**	25
C_{22}	210.6	138	218	222.6	**198.6**	25
C_{33}	281.9	162	330	298.9	**267.1**	25
C_{12}	75.7	105	109	99.1	**46.5**	25
C_{13}	19.3	121	130	46.0	**21.8**	25
C_{23}	84.2	103	108	66.5	**107.6**	25
C_{44}	88.7	26	—	100.0	**124.5**	25
C_{55}	41.7	21	—	61.7	**73.4**	25
C_{66}	59.0	21	—	89.2	**74.3**	25
B	143.0	132	149	133.47	**135.5** [12]	50

4. Calculation of physical properties

The developed MEAM interatomic potential is characterized by studying the static properties and temperature effects on some structures. Unless otherwise specified, most of the simulations have been performed with an almost cubic simulation box of $9\times4\times5$ unit cells of αU containing 720 atoms. Periodic boundary conditions are applied in all cases. MD simulations have been performed at constant volume and energy (*NVE*) or at constant pressure and temperature (*NPT*) according to the studied property. A constant simulation step of 1 fs was used at all times. The usual reference axis in which the [1 0 0], [0 1 0] and [0 0 1] crystallographic directions are correspondingly parallel to the x, y and z axes is chosen for the αU orthorhombic structure.

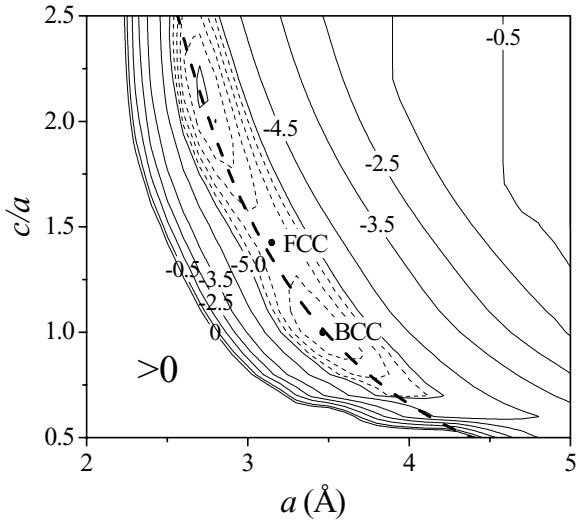

Figure 1. Calculated energy per atom (eV) for the bct structure as a function of the basal lattice parameter a and its axial ratio c/a. The positions of the equilibrium fcc and bcc structures are shown. The long dashed lines correspond to the Bain path at a constant atomic volume of 21.087 Å [3].

4.1. Bain path

Figure 1 shows a contour plot for the calculated total energy per atom as a function of the lattice parameter a and the axial ratio c/a of the bct structure for a wide range of values. Two local minima are clearly seen, one corresponding to a long bct cell with $c/a = 2.124$ (denoted as A6 in table 2) and another belonging to the bcc structure. The face-centered cubic (fcc) structure is on the saddle point between the two minima. All three points lie on a curved valley that is known as the Bain path, which is usually approximated by a transformation of the bct structure in which the c/a ratio changes at constant volume. The approximate path corresponding to the equilibrium αU atomic volume given by the present potential is indicated by the long dashed line on the contour plot. As this description of the path is not accurate, the exact positions of the fully relaxed A6, fcc and bcc structures lie close to but not exactly on that line. In his work on light actinides, Söderlind [11] studied different metastable structures in U by means of first-principles calculations. He found that the Bain path at constant atomic volume has a minimum at $c/a = 0.82$ and that the bcc ($c/a = 1$) and fcc ($c/a = 2^{1/2}$) structures were local maxima. He also predicts a local minimum at $c/a \approx 1.85$, which is not explicitly mentioned in his work. Hood *et al* [19] found similar results by using appropriate pseudopotentials for U. The present potential seems to disagree in the behavior of the bcc structure and the existence of a stable bct with $c/a < 1$, although it successfully predicts the fcc instability as well as the appearance of a stable bct lattice with $c/a \sim 2$.

4.2. Surfaces

Surface energies and layer relaxations are calculated for different crystal orientations in αU. For this purpose, a slab with more than 15 atomic layers is constructed with the appropriate orientation and using the equilibrium lattice parameters given by the MEAM potential. The surfaces are separated by an empty space that is several lattice parameters wide so that there

Table 4. Calculated surface energies γ and interlayer relaxations Δd_{ij} for the first low index surfaces.

	γ (J m^{-2})	Δd_{12} (%)	Δd_{23} (%)
(0 0 1)	2.02	+6.0	+0.8
$(0\,1\,0)_A$	2.05	–2.3	+5.7
$(0\,1\,0)_B$	2.23	+3.1	+3.5
(1 0 0)	2.27	–4.4	+11.6
(0 0 1) PAW [14]	1.8	–3.6	+1.0
Polycrystals [49]	1.0–1.49		
Fission bubbles [50]	1.0 ± 0.5		

is no interaction between periodic images. The slab is then relaxed at constant cell volume. The surface energy γ is defined as

$$\gamma = (E_{\text{slab}} - NE_{\text{c}})/2A, \tag{14}$$

where E_{slab} is the relaxed energy of the slab with N atoms and A is the area of the surface. The obtained values for three low index surfaces are shown in table 4. No reconstructions have been observed in any of the studied cases. Lattice relaxations are reported as Δd_{ij}, i.e. the change in the spacing d_{ij} between the ith and jth layers relative to the bulk. For the (0 1 0) orientation, two crystallographically different terminations are possible: one in which the spacing between the last two atomic planes is $d_{12} = 2yb$, referred to as $(0\,1\,0)_{\text{A}}$ and which is lower in energy, and another in which $d_{12} = (1 - 2y)b$, indicated as $(0\,1\,0)_{\text{B}}$. The lowest energy corresponds to the (0 0 1) orientation. Although some control of the crystallography in the epitaxial growth of αU is possible by choosing the substrate [47], the latter result seems to agree with the experimental evidence found by Opeil *et al* [48], who observed that an αU monocrystal obtained by electro-refinement grows with its c axis perpendicular to the surface. The energy value for the (0 0 1) surface is consistent with that calculated by Taylor [14] using a PAW method, differing in the relaxation sign of the first layer. The obtained values for all of the studied orientations are higher than the available experimental estimations [49, 50].

4.3. Bulk properties

MD simulations were performed to study the temperature effects on the αU structure. After a short thermalization of 1 ns at 200 K, the temperature of the simulation box of 720 atoms described above is linearly increased during 10 ns up to 2000 K. The evolution of the average atomic volume as a function of temperature is shown in figure 2. The observed abrupt changes could be identified as corresponding to the $\alpha\text{U} \leftrightarrow \gamma\text{U}$ allotropic transformation (around 1100 K) and the melting of γU (around 1650 K). The βU phase was not studied because of the short experimental temperature range of stability and because, from a technological point of view, it is not important. Periodic boundary conditions, homogeneous nucleation and size effects delay the initiation of the higher temperature phase, yielding overestimated values for these transformation temperatures [51]. A different technique is used to calculate these temperatures with better accuracy (see later).

The volume coefficient of thermal expansion can be obtained as

$$\alpha_V = \frac{1}{\Omega}\left.\frac{\partial \Omega}{\partial T}\right|_P. \tag{15}$$

By fitting the atomic volume Ω (figure 2) to a polynomial function of the temperature, a value of $\alpha_V = 16.5 \times 10^{-6}\,\text{K}^{-1}$ is obtained for αU around room temperature, which is rather

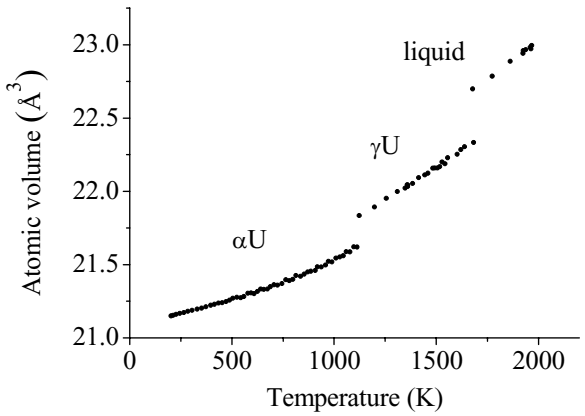

Figure 2. Evolution of the atomic volume as a function of temperature for the obtained potential.

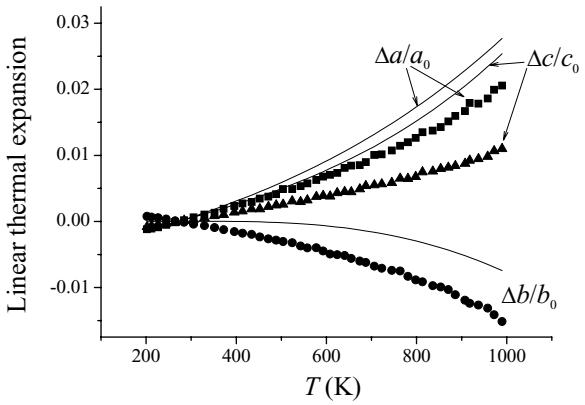

Figure 3. Linear thermal expansion for αU. The points correspond to MEAM calculated values. The lines correspond to experimental values [54].

low when compared with the experimental value of $39 \times 10^{-6}\,\mathrm{K}^{-1}$ [43]. This value is consistent with U at 17GPa as measured by Yoo *et al* [12]. For γU, the result is $\alpha_V \sim 14 \times 10^{-6}\,\mathrm{K}^{-1}$ for the bcc existence temperature range, which is also low compared with the experimental value of $\alpha_V = 22.5 \pm 1.3 \times 10^{-6}\,\mathrm{K}^{-1}$ [52]. Finally, for the liquid state $\alpha_V \sim 45 \times 10^{-6}\,\mathrm{K}^{-1}$, while $100 \pm 3 \times 10^{-6}\,\mathrm{K}^{-1}$ is obtained experimentally [53]. Although α_V differs appreciably from their experimental values, it is interesting to note that the potential captures the anomalous thermal expansion behavior of the αU lattice, i.e. the a and c lattice parameters expand while b contracts with increasing temperature (see figure 3) as in the real metal [54, 55].

Regarding the transformation $\alpha\mathrm{U} \leftrightarrow \gamma\mathrm{U}$ that occurred during the simulation shown in figure 2, the orientation relationship between the two phases is found to be $[1\,0\,0]_\alpha \parallel [1\,1\,\bar{1}]_\gamma$, $[0\,1\,0]_\alpha \parallel [1\,1\,2]_\gamma$ and $[0\,0\,1]_\alpha \parallel [1\,\bar{1}\,0]_\gamma$. Axe *et al* [56] and Söderlind [11] suggested that γU would transform to αU by means of a Burgers mechanism, passing through and rejecting the unstable hexagonal close-packed (hcp) structure at some intermediate point. The present simulations show a different transformation mechanism involving a shear of contiguous $\{1\,1\,0\}$ planes in opposite $\langle 1\,1\,1\rangle$ directions, as sketched in figure 4(*a*). The

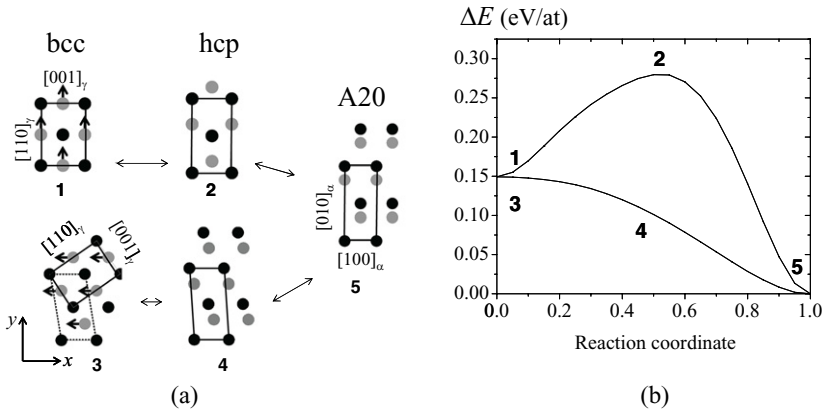

Figure 4. (*a*) Two different paths for the αU $\leftrightarrow$ γU transformation. Path 1–2–5 corresponds to the Burgers mechanism and path 3–4–5 to that suggested by the present simulation. The black (grey) circles correspond to atoms at $z = 0$ ($z = c/2$). (*b*) Energy path for both mechanisms; the numbers correspond to configurations in (*a*).

energy barrier calculated statically using the present MEAM potential is shown in figure 4(*b*) for both transformations, the Burgers mechanism and the mechanism found in the present work . Intermediate configurations are linearly interpolated between the initial and final states. The path suggested by Axe *et al* shows a finite energy barrier in both directions of the transformation, while the one observed in the reported simulations indicates that the bcc structure is unstable under this distortion. The αU/γU orientation relationship suggested by the simulations completely agrees with the experimental evidence in dilute alloys of Zr in U [57], although other authors have found different orientation relationships in dilute alloys of Ti and Mo in U [58].

The transformation temperatures T_C can be obtained more accurately using a technique developed by Morris *et al* [51]. This technique is based on simulations where the two involved phases coexist simultaneously in equilibrium, avoiding the nucleation problem altogether. Here, a long supercell of 5760 atoms is constructed for this purpose, as shown in figure 5. First, two sub-blocks of each phase are built by juxtaposing four times the same cell of the previous run of 720 atoms before and after the transformation under study (αU $\rightarrow$ γU or γU $\rightarrow$ liquid). Then, the two sub-blocks are brought into contact arbitrarily in the y direction by appropriately rescaling the x and z edges. A short thermalization at constant *NPT* is performed at $P = 0$ and an initial estimation of T_C to remove as much stress as possible. In the case of the γU $\leftrightarrow$ liquid, stresses can be effectively removed because the liquid phase can adopt any shape and follow the γU crystallography. The αU $\leftrightarrow$ γU transformation, on the other hand, will have some residual stresses due to the incommensurability of the crystal structure of each phase. When developing an EAM Zr potential, Mendelev and Ackland [59] discarded this technique for finding the hcp $\leftrightarrow$ bcc transformation parameters, as the authors claimed that a single supercell cannot be compatible with two different crystal structures. On the other hand, Smirnova *et al* [27] study the same phase changes in the development of their EAM2 potential for pure U by using this technique, although no calculation details are mentioned. In the present study, the stresses σ_{ij} on both phases have been checked to validate the use of the coexistence phase technique for this allotropic transformation. It is seen that the absolute value of the difference $|\sigma_{ij}^{\alpha} - \sigma_{ij}^{\gamma}|$ between stress components on each phase

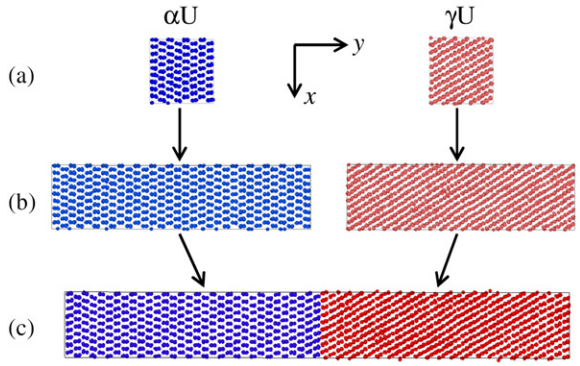

Figure 5. Construction steps of the simulation block for the study of the $\alpha U \leftrightarrow \gamma U$ allotropic transformation: (*a*) two units of 720 atoms are extracted from a previous run at linearly increasing temperatures before and after the transformation takes place; (*b*) four similar units are juxtaposed to obtain a longer cell of each phase; (*c*) finally, the two sub-blocks are brought into contact in the y direction by previously rescaling the edges of the block in the x and z directions.

Table 5. Calculated (MEAM) and experimental (Exp) transformation temperatures T_C, latent heats L and volume changes ΔV for each of the studied phase changes.

	$\alpha U \leftrightarrow \gamma U$		$\gamma U \leftrightarrow$ liquid	
	MEAM	Exp.	MEAM	Exp.
T_C (K)	972.5	$\sim$ 1075 ($P = 3.15$ GPa) [60]	1505.4	1408 [61]
L (kJ mol^{-1})	9.9	$\sim$ 30 ($P = 3.15$ GPa) [60]	6.5	8.5 [61]
ΔV (cm^3 mol^{-1})	0.12	0.8 ($P \sim 0$) [12]	0.21	0.29 [62]

does not exceed 10^{-1} GPa once equilibrium has been achieved, and therefore they are not expected to influence significantly the final value of T_C. The large block with the two phases is simulated at *NVE* under periodic boundary conditions at different volumes for 50 to 100 ps. Since energy is conserved during the simulation, the values adopted by T and P will be those corresponding to the equilibrium phase transformation at the given volume as long as the two phases are present [51]. By extrapolation to $P = 0$, the transformation temperatures T_C for each phase change can be derived. If the volume change ΔV for the transformation is known, then the latent heat L involved can be calculated by using the Clausius-Clapeyron equation, i.e. $\mathrm{d}P/\mathrm{d}T|_V = L/T_C \Delta V$. Table 5 shows all of the calculated quantities characterizing each phase change compared with the experimental values. As in nature, the $\alpha U \leftrightarrow \gamma U$ transformation is only possible for $P > 3.15$ GPa [60] and the reported values of T_C and L correspond to estimated quantities in the $\alpha/\beta/\gamma$ triple point, while that of ΔV is an extrapolation to $P = 0$ of Yoo *et al* [12].

4.4. Point defects

Formation energies of intrinsic point defects in αU are calculated by fully relaxing the atomic positions and box edges of the previously described simulation cell. Migration energy barriers are obtained using the climbing image nudged elastic band (CI-NEB) [63], as implemented in LAMMPS, with at least five system images.

The obtained value for the vacancy formation energy E_v^f in αU is much higher than those

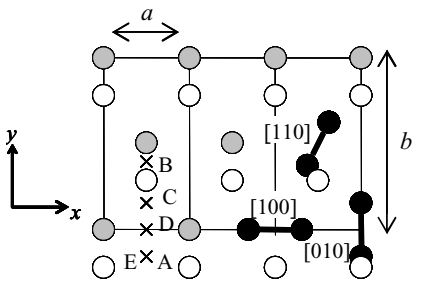

Figure 6. Some of the interstitial configurations studied in αU. Approximate site coordinates (in units of the lattice parameters) are $A = (1/2, -1/6, 0)$, $B = (1/2, 1/2 - y, 1/4)$, $C = (1/2, 1/6, 0)$, $D = (1/2, 0, 0)$ and $E = (1/2, -1/6, 1/4)$. The rest of the sites correspond to dumbbells along different crystallographic directions (not all possible configurations are shown).

calculated for other authors using first-principles techniques [14, 17, 21] (see table 1). To the authors' knowledge, there are no experimental results available in the literature to compare with. An upper bound $E_v^f < Q$ is possible to establish, assuming that $Q = E_v^f + E_v^m$ holds, where $Q = 1.7 - 1.9$ eV is the experimental activation energy for self-diffusion in αU [64]. In the case of γU, a fully relaxed static calculation with the present potential is not possible because the extraction of an atom from the perfect structure completely destabilizes the lattice which decays to βNp, a bcc related structure [11]. Since temperature effects are important to the bcc stability, MD simulations at constant *NPT* have been performed for 10^3 ps at several temperatures between 1000 and 1500 K. A simulation block of $8 \times 8 \times 8$ bcc unit cells containing $N = 1024$ atoms was used. Simulations of the lattice with and without a vacancy allow us to estimate the formation energy as $E_v^f = \langle E_{N-1} \rangle - (N-1)\langle E_N \rangle / N$, where $\langle E_N \rangle$ is the average energy along the MD run for the system with N atoms. Unfortunately, for the chosen simulation times the statistical errors in the determination of the different $\langle E_N \rangle$ are not small enough to establish a confident value of E_v^f. Large variations with temperature only allow us to determine values in the range $1.3\,\text{eV} < E_v^f < 2.6\,\text{eV}$. This range is close to that measured by the positron annihilation technique of Matter *et al* [65], 1.2 ± 0.25 eV, and even closer to that recently reported by Lund *et al* [66], 1.6 ± 0.16 eV. First-principles calculations of Xiang *et al* [15] produce a lower value of $E_v^f = 1.08$ eV, while Beeler *et al* [17] obtain 1.32 and 1.38 eV with different density functional approximations.

Vacancy jumps in αU up to fourth neighbors are calculated and their migration energies E_v^m are reported in table 1. Jumps (1) and (2) allow the vacancy to move along the c and a axes, respectively, and contribute to the mobility on the corrugated (0 1 0) planes. Jump (3) is a basal jump along the [1 1 0] direction while jump (4) has components along the three axes [25]. Even when only jumps (1) and (2) are included in the fitting process, jumps (3) and (4) yield corresponding values very close to those obtained by Huang and Wirth [21].

Interstitial sites in αU have been investigated by several authors [67–69]. Some of these configurations, as well as split dumbbell self-interstitials, are shown in figure 6. Note that dumbbells with similar indexes are not equivalent due to orthorhombic symmetry and have to be studied independently. The interstitial formation energies calculated with the present MEAM potential for all of the studied configurations are shown in table 6. The same configurations are also studied with the EAM2 potential for comparison. All configurations that are marked as unstable decay to one of the three stable configurations found: the dumbbells [1 1 0] and [0 0 1] and the interstitial E, the former corresponding to the ground state. A different situation is

Table 6. Self-interstitial formation energies (eV) for configurations in figure 6. Results obtained with the EAM2 potential [27] and first-principles values from the literature are also reported.

Config.	MEAM	EAM2 [27]	First principles
A	Unstable	2.729	
B	Unstable	Unstable	
C	Unstable	2.766	
D	Unstable	2.852	
E	3.960	Unstable	4.42 [21]–4.28 [29]
[1 0 0]	Unstable	2.868	
[0 1 0]	Unstable	Unstable	
[0 0 1]	3.956	2.714	
[1 1 0]	3.436	Unstable	
[1 0 1]	Unstable	2.829	
[0 1 1]	Unstable	2.730	

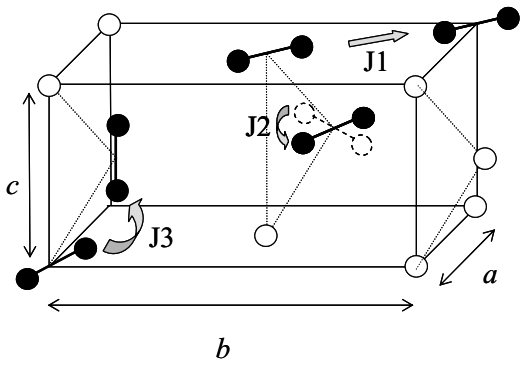

Figure 7. Interstitial jumps found in αU. The full circles indicate the dumbbell configurations.

found for the EAM2 potential, although both interaction schemes agree in yielding the [0 0 1] dumbbell as one of the configurations of lowest energy. First-principles studies of Huang and Wirth [21] stated that the lowest energy configuration found corresponds to the E site, with a formation energy 10% higher than that found with the present potential. A slightly lower value is calculated by Li *et al* [29] using the same calculation method.

Regarding interstitial migration, three elemental migration paths necessary for 3D diffusion are proposed in figure 7, based on the [0 0 1] and [1 1 0] dumbbell configurations. Their migration energies, calculated through the CI-NEB technique, are 0.025 eV for jump J1, 0.142 eV for jump J2 and 0.684 eV (0.163 eV) for jump [1 1 0] $\rightarrow$ [0 0 1] ([0 0 1] $\rightarrow$ [1 1 0]) in the case of J3. An analysis of these migration energies shows that the interstitial diffusivity in the (0 0 1) plane will be much faster than in the perpendicular direction. This will be evident in the MD simulations of interstitials in αU reported in the next section.

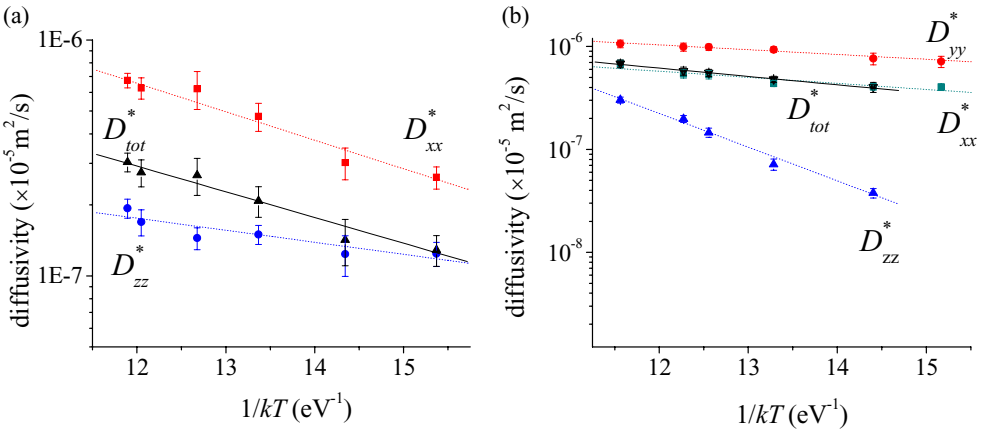

Figure 8. Diffusivities by (*a*) vacancy and (*b*) interstitial mechanisms in αU. The full line indicates the total diffusivity D^*_{tot}.

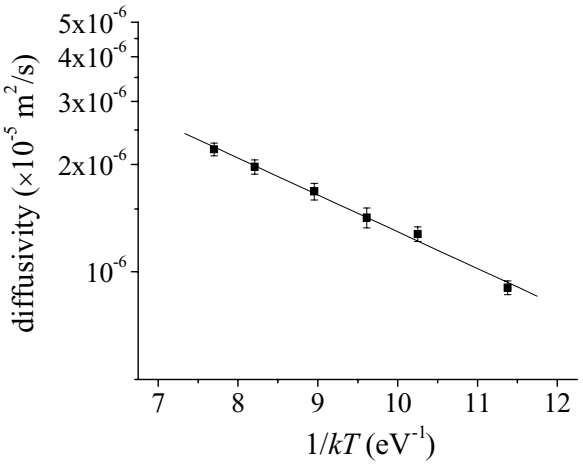

Figure 9. Diffusivity by vacancy mechanism in γU.

4.5. Diffusion

Point defect mobility as a function of temperature is studied by means of MD simulations. A vacancy or an interstitial is generated and the system is allowed to evolve at constant *NPT* ($P = 0$) for a time t long enough ($t = 10^3$ ps) to reach equilibrium. Then, the simulation is continued at constant equilibrium volume for a time substantially greater (10^4 ps for interstitials and 4×10^4 ps for vacancies). In this second stage, the mean square displacement of atoms due to the exchange with the defect is recorded. The resulting values of $D^*_{xx} = \lim_{t\to\infty} \langle x^2 \rangle / 2t$ for each component of the diffusivity along each principal direction x are shown as Arrhenius plots in figures 8 and 9 for the vacancy and interstitial mechanisms in αU (750 K $\leqslant T \leqslant$ 1000 K) and for the vacancy mechanism in γU (1000 K $\leqslant T \leqslant$ 1500 K), respectively. Self-interstitial diffusivity in γU is excluded from the present study. The results show that the vacancy moves faster along the a and c axes than along b in αU. Substantially longer simulation times

Table 7. Migration energies for the vacancy E_v^m and interstitial E_i^m mechanisms in αU.

	E_v^m (eV)	E_i^m (eV)
x	0.29 ± 0.03	0.14 ± 0.03
y	—	0.11 ± 0.04
z	0.11 ± 0.04	0.77 ± 0.04
Total	0.25 ± 0.05	0.19 ± 0.05

than those reached here are needed to gather enough statistics to resolve the D^*_{yy} component. It could only be established that it is at least one order of magnitude lower than D^*_{xx} and D^*_{zz} for the whole temperature range. Self-interstitials are faster than vacancies and their mobility is greater in the (0 0 1) basal planes than along the c axis. Based on bond lengths, Seigle and Opinsky [70] predicted that the vacancy would move faster in the corrugated (0 1 0) planes where covalent bonds are stronger. Meanwhile, they proposed that the self-interstitial would move almost isotropically. However, it should be kept in mind that their study only considers the atomic jump through interstitial holes in αU and does not take into account dumbbell configurations, which are more anisotropic. In tracer diffusion experiments on αU, it is observed that $D_{xx} \sim D_{zz} \gg D_{yy}$ [71] in agreement with the present results for the vacancy mechanism. Neutron irradiation experiments also show a large growth anisotropy in which a crystal of αU increases its length in the [0 1 0] direction and decreases in the [1 0 0] direction, while in the transverse [0 0 1] direction no dimensional changes are observed [72]. The work of Gonser [73] is based on an increased mobility of the vacancy in the [1 0 0] direction and the interstitial in the [0 1 0] direction, similar to that found here, to explain these dimensional changes. The vacancy and self-interstitial migration energies along the αU principal axes, obtained by fitting the data to $D^*(T) = D_0^* \exp(-E^m/kT)$, are reported on table 7. The large uncertainties are indicative of the difficulty in achieving acceptable statistics, even with the relatively long simulation times used. There is a good correspondence with the jump energy barriers calculated statically by means of the CI-NEB method of the previous section.

The vacancy diffusivity in γU does not show any signs of appreciable curvature in the Arrhenius plot of figure 9. Diffusion in γU has been classified as anomalous more due to the low values of D_0 and Q rather than the curvature, as occurs in other metals like Zr and Ti in their bcc high-temperature phase [74]. Although some controversy still exists, a temperature dependence of E_v^f has been proposed to explain this behavior [65], in opposition to the E_v^m temperature dependence found in other normal bcc metals like tungsten [75]. The vacancy migration energy in γU extracted from figure 8 is 0.23 ± 0.01 eV. Adding the above obtained value $E_v^f = 1.7 \pm 0.6$ eV results in an activation energy of $Q = 1.9 \pm 0.6$ eV, which is much higher than the experimental value of 1.15 eV [64].

5. Summary and conclusions

The present paper provides an interatomic MEAM-type potential to model metallic U. Many physical properties are reasonably reproduced, but care should be exercised when using this potential in other studies than those approaches herein. The parameters of the interaction fit experimental and/or first-principles values extracted from the literature, covering a wide range of structural and elastic properties of the low-temperature phase αU and many other metastable competing structures. This provides the potential with one of its main characteristics, which is the stability achieved at finite temperatures for αU. Other MEAM potentials reported in the

literature [28] lack physical accuracy as they do not give the αU phase as the lowest energy state.

The potential reproduces a simplified $\alpha\text{U} \leftrightarrow \gamma\text{U}$ allotropic transformation and melting at temperatures relatively close to the experiment. Previous EAM potentials [23–25, 27] are similar to the present one in that they all predict that αU is the ground state and γU and liquid phases show up at increasing temperatures, although they tend to underestimate the $\alpha\text{U} \leftrightarrow \gamma\text{U}$ transformation temperature further. The simulations performed suggest a new alternative mechanism for this allotropic transformation, different from that of Burgers which was proposed in the literature but still not confirmed [11, 56]. Unfortunately, the potential reproduces a βU energy higher than that of αU and γU for the studied temperature range. For this reason, we do not advise using this potential to study βU phase properties.

Similarly, the obtained potential is not suitable for simulations at finite pressures in αU as it does not give the correct dependence of the c/a ratio as a function of pressure [76], and therefore will not be able to describe properly transitions in U at high pressures.

Linear expansion agrees qualitatively with experimental observation in αU, i.e. the contraction of b and expansion of a and c lattice parameters with increasing temperature, although it falls short of the experimental value in each of the studied phases, α, γ and liquid U, by half.

Regarding αU surface properties, the (0 0 1) surface energy show good agreement when it is compared with Taylor first-principles calculations [14], but lattice relaxations of the first layers have the opposite sign.

The resultant description of the intrinsic point defects and their anisotropic mobility in αU shows good agreement with the observed dimensional changes suffered under neutron irradiation [73]. Finally, no detectable curvature was found in the Arrhenius plot for the vacancy diffusivity in γU and we obtained values of Q that are higher than experiments. All in all, the present potential provides a rather good description of the pure metal at finite temperatures, even when its parameters are fitted to properties at $T = 0$ K. This potential will be used to construct appropriate interactions for Al–Mo–U ternary alloys in future work.

Acknowledgment

The authors wish to acknowledge the support of projects PIP 804/10 (CONICET) and CO57 (UNSAM).

References

[1] Lundberg L 1989 *J. Nucl. Mater.* **167** 64–5
[2] Snelgrove J, Hofman G, Meyer M, Trybus C and Wiencek T 1997 *Nucl. Eng. Des.* **178** 119–26
[3] Meyer M K, Hofman G L, Hayes S L, Clark C R, Wiencek T C, Snelgrove J L, Strain R V and Kim K-H 2002 *J. Nucl. Mater.* **304** 221–36
[4] Kassner M E, Adler P H, Adamson M G and Peterson D E 1989 *J. Nucl. Mater.* **167** 160–8
[5] Van den Berghe S, Van Renterghem W and Leenaers A 2008 *J. Nucl. Mater.* **375** 340–6
[6] Ryu H J, Kim Y S and Hofman G L 2009 *J. Nucl. Mater.* **385** 623–8
[7] Smith J L and Kmetko E A 1983 *J. Less-Common Met.* **90** 83–8
[8] Lander G H, Fisher E S and Bader S D 1994 *Adv. Phys.* **43** 1–111
[9] http://cst-www.nrl.navy.mil/lattice/index.html
[10] Söderlind P, Eriksson O, Johansson B and Wills J M 1994 *Phys. Rev.* B **50** 7291–4
[11] Söderlind P 1998 *Adv. Phys.* **47** 959
[12] Yoo C, Cynn H and Söderlind P 1998 *Phys. Rev.* B **57** 10359–62
[13] Söderlind P 2002 *Phys. Rev.* B **66** 085113
[14] Taylor C D 2008 *Phys. Rev.* B **77** 094119

Taylor C D 2009 *Phys. Rev.* B **80** 149906 (erratum)
[15] Xiang S, Huang H and Hsiung L 2008 *J. Nucl. Mater.* **375** 113–9
[16] Li J H, Ren Q B, Lu C H, Lu L, Dai Y and Liu B X 2012 *J. Alloys Compounds* **516** 139–43
[17] Beeler B, Good B, Rashkeev S, Deo C, Baskes M and Okuniewski M 2010 *J. Phys.: Condens. Matter* **22** 505703
[18] Beeler B, Deo C, Baskes M and Okuniewski M 2013 *J. Nucl. Mater.* **433** 143–51
[19] Hood R Q, Yang L H and Moriarty J A 2008 *Phys. Rev.* B **78** 024116
[20] Söderlind P, Grabowski B, Yang L, Landa A, Björkman T, Souvatzis P and Eriksson O 2012 *Phys. Rev.* B **85** 060301
[21] Huang G Y and Wirth B D 2011 *J. Phys.: Condens. Matter* **23** 205402
Huang G Y and Wirth B D 2012 *J. Phys.: Condens. Matter* **24** 415404
[22] Landa A, Söderlind P and Turchi P E A 2011 *J. Nucl. Mater.* **414** 132–7
[23] Pascuet M I, Fernández J R and Monti A M 2007 *Anal. AFA* **19** 40–5
[24] Pascuet M I, Fernández J R and Monti A M 2008 *Proc. 4th Int. Conf. on Multiscale Materials Modeling (Tallahassee, FL)* pp 437–40
[25] Pascuet M I, Bonny G and Fernández J R 2012 *J. Nucl. Mater.* **424** 158–63
[26] Belashchenko D K, Smirnova D E and Ostrovski O I 2010 *High Temp.* **48** 363–75
[27] Smirnova D E, Starikov S V and Stegailov V V 2012 *J. Phys.: Condens. Matter* **24** 015702
[28] Beeler B, Deo C, Baskes M and Okuniewski M 2012 *J. Phys.: Condens. Matter* **24** 075401
[29] Li Y, Shan T, Liang T, Sinnot S and Phillpot S 2012 *J. Phys.: Condens. Matter* **24** 235403
[30] Baskes M I 1992 *Phys. Rev.* B **46** 2727–42
[31] Daw M S and Baskes M I 1984 *Phys. Rev.* B **29** 6443–53
[32] Finnis M W and Sinclair J E 1984 *Phil. Mag.* A **50** 45–55
[33] Plimpton S J 1995 *J. Comput. Phys.* **117** 1–19; http://lammps.sandia.gov
[34] Gullett P M, Wagner G J, Slepoy A, Horstemeyer M F, Fang H, Li M and Baskes M I 2003 Numerical tools for atomistic simulations *SANDIA Report* 2003–8782
[35] Baskes M I 1997 *Mater. Chem. Phys.* **50** 152–8
[36] Rose J H, Smith J R, Guinea F and Ferrante J 1984 *Phys. Rev.* B **29** 2963–9
[37] Lee B-J and Baskes M I 2000 *Phys. Rev.* B **62** 8564–7
Lee B-J, Baskes M I, Kim H and Yang K Ch 2001 *Phys. Rev.* B **64** 184102
[38] Teukolsky S A, Vetterling W T and Flannery B P 1997 *Numerical Recipes in Fortran 77: The Art of Scientific Computing* ed W H Press (New York: Cambridge University Press)
[39] Taylor C D 2009 *Phys. Rev.* B **80** 024104
[40] Kniznik L, Alonso P R, Gargano P H, Forti M D and Rubiolo G H 2012 *Proc. Mater. Sci.* **1** 514–19
[41] Crocombette J P, Jollet F, Thien N L and Petit T 2001 *Phys. Rev.* B **64** 104107
[42] Garcés J E, Marino A C and Bozzolo G 2003 *Appl. Surf. Sci.* **219** 47–55
[43] Barrett C S, Mueller M H and Hitterman R L 1963 *Phys. Rev.* **129** 625
[44] Kittel C 1986 *Introduction to Solid State Physics* (New York: Wiley Interscience)
[45] Wilson A S and Rundle R E 1949 *Acta Crystallogr.* **2** 126–7
[46] Fisher E S and McSkimin H J 1961 *Phys. Rev.* B **124** 67–70
[47] Ward R C C, Cowley R A, Ling N, Goetze W, Lander G H and Stirling W G 2008 *J. Phys.: Condens. Matter* **20** 135003
[48] Opeil C P *et al* 2006 *Phys. Rev.* B **73** 165109
[49] Taylor J W 1955 *J. Nucl. Mater.* **2** 15–30
[50] Bainbridge J E and Hudson B 1965 *J. Nucl. Mater.* **17** 237–44
[51] Morris J R, Wang C Z, Ho K M and Chan C T 1994 *Phys. Rev.* B **49** 3109
[52] Klepfer H H and Chiotti P 1957 *Report* No ISC-893, Iowa State College
[53] Sheldon R I and Mulford R N R 1991 *J. Nucl. Mater.* **185** 297–8
[54] Chiswick H H, Dwight A E, Lloyd L T, Nevitt M V and Zegler S T 1958 *Proc. 2nd U.N. Int. Conf. on Peaceful uses of Atomic Energy (Geneva, Switzerland)* p 394
[55] Lloyd L T and Barrett C S 1966 *J. Nucl. Mater.* **18** 55–9
[56] Axe J D, Grübel G and Lander G H 1994 *J. Alloys Compounds* **213/214** 262–7
[57] Hato B A 1966 *J. Nucl. Mater.* **19** 133–41

[58] Speer J G and Edmonds D V 1988 *Acta Metall.* **36** 1015–33
[59] Mendelev M I and Ackland G J 2007 *Phil. Mag. Lett.* **87** 349–59
[60] Klement W Jr, Jayaraman A and Kennedy G C 1963 *Phys. Rev.* **129** 1971–5
[61] Weeks M E 2003 *Discovery of the Elements* (Whitefish, MT: Kessinger)
[62] Rohr W G and Wittenberg L J 1970 *J. Phys. Chem.* **74** 1151
[63] Henkelman G, Uberuaga B P and Jónsson H 2000 *J. Chem. Phys.* **113** 9901–4
[64] Neumann G and Tuijn C 2009 *Self-Diffusion and Impurity Diffusion in Pure Metals: Handbook of Experimental Data* (*Pergamon Materials Series* vol 14) (Oxford: Pergamon) chapter 10
[65] Matter H, Winter J and Triftshäuser W 1980 *J. Nucl. Mater.* **88** 273–8
[66] Lund K R, Lynn K G, Weber M H and Okuniewski M A 2013 *J. Phys.: Conf. Ser.* **443** 012021
[67] Opinsky A J 1954 *J. Met.* **6** 913–14
[68] Sutton A L, Eeles W T and Price A M 1962 *Proc. 5th Colloquium of the UKAEA Diffraction Analysis Conf.* ed M H Rand (Bornemouth, UK: Harwell) *Report* AERE R.3818, p 45
[69] Rao C N and Tangri K 1963 *Trans. Indian Inst. Met.* **16** 93
[70] Seigle L L and Opinsky A J 1957 *Nucl. Sci. Eng.* **2** 38
[71] Rothman S J, Hines J J, Gray Jr and Harkness A L 1962 *J. Appl. Phys.* **33** 2113–16
[72] Cheboraterv N T 1998 *At. Energy* **85** 438–46
[73] Gonser U 1960 *J. Nucl. Mater.* **2** 43–50
[74] Peterson N L and Rothman S J 1964 *Phys. Rev.* **136** 842–8
[75] Landolt-Börnstein 1991 *Numerical Data and Functional Relationships in Science and Technology* New Series vol III/25, ed H Ullmaier (Berlin: Springer)
[76] Akella J, Weir S, Wills J M and Söderlind P 1997 *J. Phys.: Condens. Matter* **9** L549-555